Physics of the Earth and Planetary Interiors 366 (2025) 107410

Contents lists available at ScienceDirect

Physics of the Earth and Planetary Interiors

journal homepage: www.elsevier.com/locate/pepi

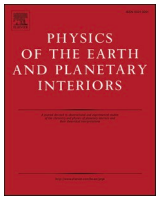

The source process of the 2014 Jinggu earthquake in Yunnan, China

Junlei Chen [a,*], Yan Li [a], Jinlai Hao [b,d], Tao Xu [c,d]

[a] Faculty of Public Security and Emergency Management, Kunming University of Science and Technology, No.253 Xuefu Road, Kunming 650031, Yunnan Province, China
[b] Key Laboratory of Earth and Planetary Physics, Institute of Geology and Geophysics, Chinese Academy of Sciences, No.19 Beitucheng Western Road, Chaoyang District, Beijing 100029, China
[c] Key Laboratory of Mineral Resources, Institute of Geology and Geophysics, Chinese Academy of Sciences, No.19 Beitucheng Western Road, Chaoyang District, Beijing 100029, China
[d] Innovation Academy for Earth Science, Chinese Academy of Sciences, No.19 Beitucheng Western Road, Chaoyang District, Beijing 100101, China

ARTICLE INFO

Keywords:
Jinggu earthquake
Rupture process
Focal mechanism

ABSTRACT

The 2014 Jinggu M_w 6.0 earthquake occurred in the complex conjugate fault system of the Southwest Yunnan Block, comprised of NNW-trending and NNE-trending faults. We relocated the mainshock's hypocenter and inverted the focal mechanisms of earthquakes greater than M 3.5 and the mainshock's rupture process to study the earthquake sequence's source process. The relocation of the mainshock's hypocenter was determined to be at 100.47°E, 23.40°N, and 9.3 km. The focal mechanism of the mainshock is 150°/76°/179°(strike/dip/rake). There are 21 strike-slip earthquakes, 2 normal aftershocks, and 2 thrust aftershocks. The average dip angle of the Jinggu earthquake sequence is 78.75°. The Jinggu earthquake was a single-fault bilateral rupture event. The peak slip, average rake, and slip rate of the mainshock are 0.56 m, 182°, and 2.12 km/s, respectively. The main slip patch of the mainshock slip model was at 4 km in the 150° direction from the epicenter with a depth ranging from 4 km to 9 km. Ninety percent of the energy was released within the first 5.8 s. The Jinggu earthquake sequence may consist of ruptures on two fault planes dominated by the mainshock and two M_w 5.5 aftershocks occurring within the conjugate fault system.

1. Introduction

According to the China Earthquake Networks Center (CENC) report, at 13:49:39 UTC on October 7, 2014, an M_S 6.6 earthquake (referred to as the Jinggu earthquake) occurred in Yunnan Province, China. The hypocenter was located at 100.46°E, 23.39°N, with a focal depth of 8 km. The Jinggu earthquake occurred in the Wuliangshan fault zone, which is located on the southwestern boundary of the Chuan-Dian Rhombic Block. On August 3 of the same year, another earthquake, referred to as the Ludian earthquake, struck the eastern boundary of the Chuan-Dian Rhombic block, with a magnitude (M_S 6.5) comparable to that of the Jinggu earthquake (Chen et al., 2024). The Jinggu earthquake had a magnitude up to M_S 6.6, but its impact and destructiveness on the surface were relatively minor. According to the strong-motion records and damage assessments of the Jinggu earthquake (Xu et al., 2018), the highest intensity of the Jinggu earthquake was VIII, and a Peak Ground Acceleration (PGA) of 0.64 g (at station code 053JYP; component N; epicenter distance 6.9 km). The Jinggu earthquake resulted in 1 death, 324 injuries, and economic losses of ¥18.9682 hundred million, (Jia et al., 2016). The differences in the damage caused by the earthquake ruptures from the two earthquakes require further exploration.

The Wuliangshan fault zone, where the epicenter is located, consists of the Mohei fault, Puer fault, Puwen fault, and Jinggu-Yunxian fault (Wen et al., 2022). Meanwhile, the Wuliangshan Fault Zone is situated within the Southwestern Yunnan Block (Fig. 1). The Southwest Yunnan Block is located to the west of the Red River Fault, which serves as a major boundary fault zone for the Chuan-Dian Rhombic Block (Xu et al., 2014). The Southwest Yunnan Block and the Chuan-Dian Rhombic Block together comprise the southeastern margin of the Tibet Plateau. The Southwest Yunnan Block is characterized by the development of two main sets of active fault zones. One set consists of northeast-trending (NNE) arc-shaped sinistral faults, including the major Dayingjiang Fault, Ruili Fault, Nantinghe Fault, Menglian Fault, and Jinghong Fault, which exhibit a concentric circular arc pattern with the eastern Himalayan syntaxis as the center; the other set consists of northwest-trending (NNW) dextral faults that intersect perpendicularly with the northeast-

* Corresponding author.
E-mail addresses: jlchen@kust.edu.cn (J. Chen), haojl@mail.iggcas.ac.cn (J. Hao), xutao@mail.iggcas.ac.cn (T. Xu).

https://doi.org/10.1016/j.pepi.2025.107410
Received 26 November 2024; Received in revised form 22 May 2025; Accepted 12 June 2025
Available online 15 June 2025

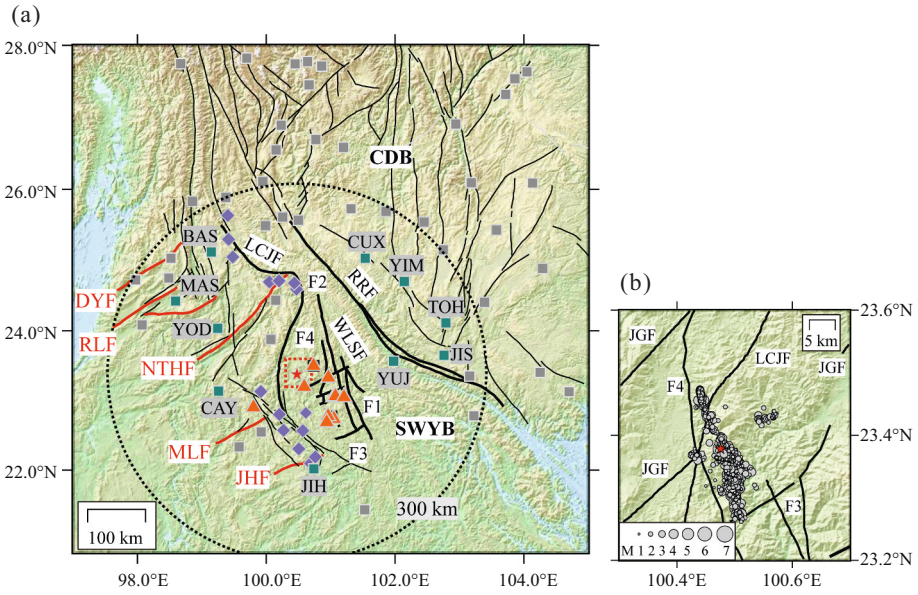

Fig. 1. The tectonic background of the Jinggu earthquake sequence. (a) The gray and dark green squares (labeled) represent broadband seismic stations used for the mainshock relocation and finite-fault inversion, respectively. The purple diamonds indicate the short-period reservoir seismic stations. The orange triangles represent the strong-motion stations. The black lines denote the NNW faults in the research area: F1 is the Mohei fault; F2 is the Puer fault; F3 is the Puwen fault; F4 is the Jinggu-Yunxian fault; RRF is the Red River fault; WLSF is Wuliangshan fault; LCJF is Lanchangjiang fault. The red lines denote the NNE faults: DYF is Dayingjiang fault; RLF is Ruili fault; NTHF is Nantinghe fault; MLF is Menglian fault; JHF is Jinghong fault. The abbreviations denote the tectonic units: CDB is Chuan-Dian block; SWYB is Southwest Yunnan block. The circle marks the epicentral distance of 300 km. (b) The dots denote the Jinggu earthquake sequence, With the red star marking the mainshock. JGF is Jinggu fault. F3, F4, LCJF are the same as (a). (For interpretation of the references to color in this figure legend, the reader is referred to the web version of this article.)

trending arc-shaped faults, including the major Lincang Fault, Lanchangjiang Fault, and Wuliangshan Fault (Shi et al., 2016).

The 2014 Jinggu earthquake's seismogenic mechanism, operating within a conjugate fault system, has been extensively studied through multidisciplinary analyses. Surface rupture characteristics and regional seismotectonic assessments initially identified the northwest-trending Jinggu-Yunxian Fault as the causative structure (Chang et al., 2016). Subsequent aftershock relocations and focal mechanism solutions revealed a northwest-trending linear rupture pattern dominated by dextral strike-slip motion (Xu et al., 2015). However, the relocation based on waveform cross-correlation further delineated a bifurcated aftershock cluster southeast of the mainshock (Wang et al., 2018). The interaction mechanisms between conjugate fault systems and the Jinggu earthquake sequences, particularly their control over rupture propagation patterns and stress release dynamics, remain unresolved. The relocation of the mainshock's hypocenter, the inversion of the point source mechanisms of earthquake sequence, and the inversion of the mainshock's rupture process can indeed provide valuable insights into the seismic source physics (Zhang et al., 2019; Yue et al., 2022; Gong et al., 2022; Li et al., 2022; Liu et al., 2022; Zhang et al., 2022; Cheng et al., 2023; Guo et al., 2023; Liang et al., 2023; C. Liu et al., 2023; Y. Liu et al., 2023). In this study, the regional broadband seismic data and the local short-period seismic data were used to relocate the mainshock's hypocenter. The regional broadband seismic data were applied to invert the focal mechanisms of earthquakes with a magnitude greater than *M* 3.5. The unclipped regional broadband seismic data and local strong-motion data were utilized to restrain the rupture process of the mainshock. This investigation aimed to explore the source process of the Jinggu earthquake sequence and to provide insights into the earthquake rupture mechanism within the conjugate fault system of the Southwest Yunnan Block, as well as the relationship between the source process and the relatively minor disaster impact.

2. Relocation of the mainshock

In the inversion of the finite-fault rupture process, the hypocenter is a prior information that needs to be used. Therefore, we used a grid search method (Ye et al., 2017) to test the accuracy of the mainshock's hypocenter. Due to the interference of the *P* coda wave on *S*-wave arrival times, which increases errors in manual picking, this study only utilizes *P*-wave first arrivals to constrain the source location. In the test, the *Z*-component *P*-wave first arrivals were manually picked from 48 stations of the Yunnan Broadband Seismic Network and 26 stations of the Yunnan Short-Period Reservoir Seismic Network (Fig. S1). Then, the theoretical *P*-wave first arrivals of each grid were calculated using *TauP* (Crotwell et al., 1999), and a modified *Crust* 1.0 velocity model (Laske et al., 2013; Y. Liu et al., 2023; Wu et al., 2024; Table S1; Text S1). When calculating the theoretical arrival times, the epicentral distance, depth intervals, and initial epicenter were set to 0.1°, 0.5 km, 100.46°E, and 23.39°N, respectively. The grid with the smallest residuals is the relocated epicenter. Then, using the relocated epicenter, the same strategy was employed to determine the source depth. The parameter domain and intervals for the grid search are shown in Table S2. After relocation (Fig. S2), the epicenter of the mainshock was determined to be at 100.47°E, 23.40°N, which is very close to the epicenter obtained through double-difference relocation (Wang et al., 2018) used in our rupture process inversion, specifically 100.48°E, 23.38°N. However, the source depth of the grid search (15 km) and double-difference relocation (15.384 km) were deeper than the depth reported by CENC (8 km).

Due to the poor constraint on source depth from the *P*-wave first arrivals, we employed a depth scanning algorithm (DSA) based on depth phases (Yuan et al., 2020) to obtain the source depth of the mainshock. The detailed information about DSA was described in the supplementary text S2. The instrument response was removed from the three-component of broadband seismic data. The short-period velocity records of reservoir stations were integrated into the displacement records. Subsequently, all data were deaveraged, detrended, and the horizontal components were rotated to radial and transverse

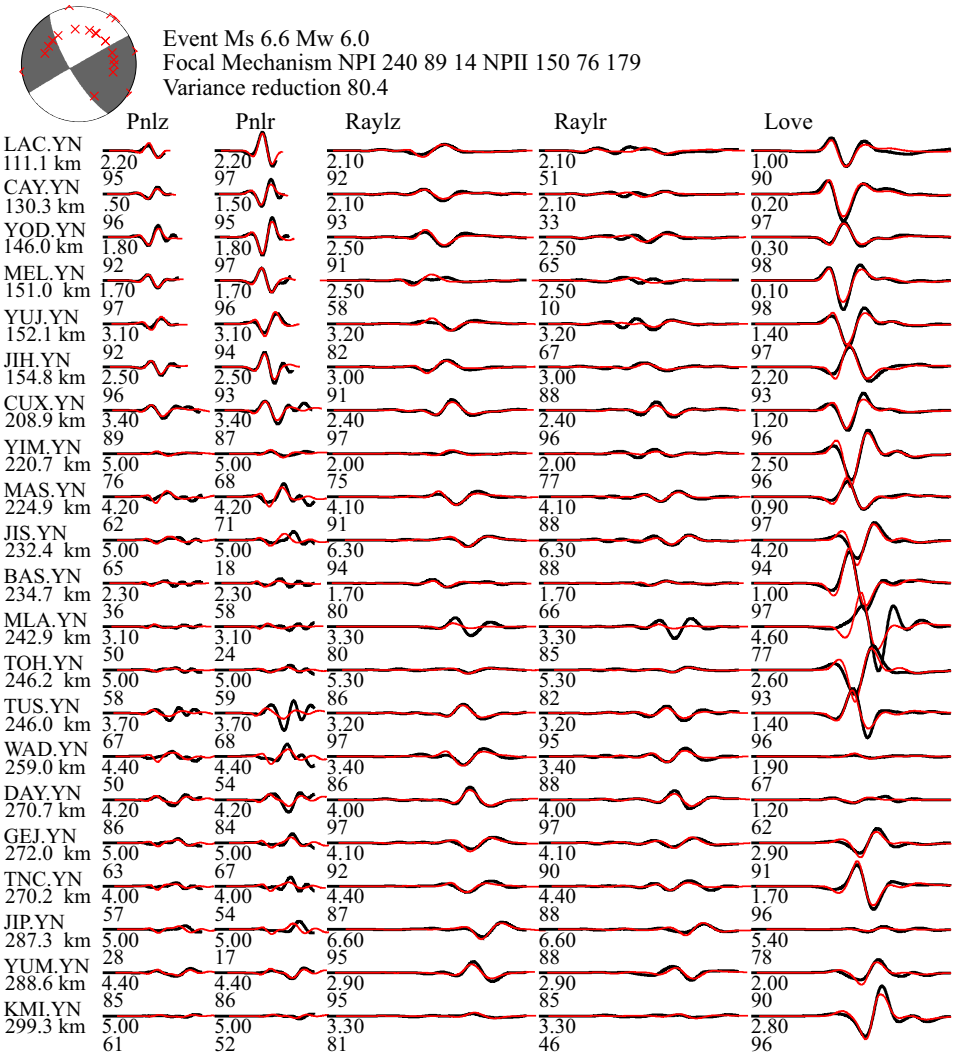

Fig. 2. The focal mechanism and waveform fitting of the Jinggu earthquake. The station name and epicentral distance (km) are marked on the left of observed records (black), and synthetic waveforms (red) are denoted. The values under the waveforms denote the time shift and cross-correlation coefficient. (For interpretation of the references to color in this figure legend, the reader is referred to the web version of this article.)

components. After using the DSA method, nine stations, including YJT station (Fig. S3, S4), were selected as the optimal stations for depth localization. The depth phases used in our source depth analysis are documented in Table S3. The best estimated focal depth obtained from the scan is 9.3 km (Fig. S5).

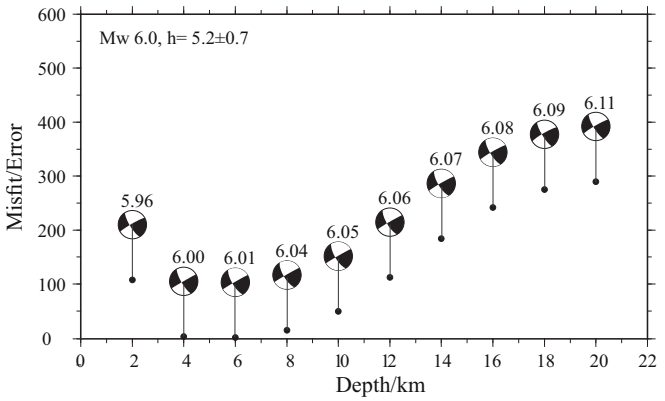

Fig. 3. The mainshock focal mechanism solutions and misfits with different fitting depths. The depth *h* represents the best-fit value with the error margin. The value on the top of the focal mechanism is the moment magnitude.

3. Focal mechanism solutions

We inverted the source mechanism solutions of 26 earthquakes with $M > 3.5$ from the 2014 Jinggu earthquake sequence between October 7 and December 9 (Table S4). We adapted the gCAP method (Zhu and Ben-Zion, 2013) to invert the focal mechanism. The regional broadband seismic data were obtained from the International Earthquake Science Data Center (esdc.ac.cn). The distribution of stations is shown in Fig. 1a. The stations with epicentral distances of less than 300 km were utilized in the inversion. In this study, we use the *F-K* method (Zhu and Rivera, 2002) to calculate Green's functions based on the 1D velocity model (Table S1). After deaveraging, detrending, and removing response, the raw horizontal displacement records were rotated to radial and tangential components. In the inversion, the synthetic and observed seismograms were filtered with the same frequency band. The *Pnl* and surface waves were filtered by the band of 0.05 Hz–0.2 Hz and 0.02 Hz–0.1 Hz, respectively. The window lengths of *Pnl* and surface waves were 35 s and 70 s, respectively. The domains of the source mechanism parameters ($0 \le \theta < 360°$, $0 \le \delta \le 90°$, $-180° \le \lambda \le 180°$) were searched by the step of 5°. The searching depth ranged from 2 km to 20 km, with a depth step of 1 km.

We selected 21 regional broadband stations with unclipped seismic waveforms to participate in the mainshock mechanism inversion (Fig. S6). In our inversion, the regional broadband data were used, and approximately 64 % of waveform fitting cross-correlation coefficients were above 80 % (Fig. 2). The focal mechanism of the mainshock is 240°/89°/14° (θ, δ, λ) of the nodal plane (NP) I, and 150°/76°/179° of NP II (Fig. 2). Our mainshock mechanism is consistent with the results obtained using regional broadband seismic data (Xu et al., 2014; Wang et al., 2018; Wang et al., 2019). The mechanisms of GCMT derive from centroid moment tensor, rather than a focal mechanism associated with the nucleation point of the rupture. The P-axis direction obtained from the GCMT is NNE, which is opposite to the SSW direction of the P-axis derived from the point source mechanisms (Fig. S7). The moment magnitude of the mainshock achieved through our mechanism inversion is M_w 6.0 (Kanamori and Anderson, 1975; Kanamori, 1977). Our moment magnitude result is slightly lower than the M_w 6.1 estimated from seismic energy based on the source spectrum (Song et al., 2020) and other studies (Table S5). In this study, the best-fit depth of the mainshock was found to be 5.2 km (Fig. 3).

The focal mechanisms of 24 aftershocks with $M > 3.5$ were derived. In the results of the inversion, there are 20 strike-slip earthquakes, 2 normal aftershocks, and 2 thrust aftershocks, in which 83 % of the aftershocks are strike-slip earthquakes (Table S6). The aftershock focal mechanism solutions include two M_w 5.5 largest aftershocks of the Jinggu earthquake sequence (Table S7). Based on the precise locations of the determined aftershocks (Wang et al., 2018), we observed that the distance between these two largest aftershocks was only 1.91 km. Our focal mechanism solutions reveal that these two aftershocks exhibit relatively similar focal mechanisms, moment magnitude, and depth.

4. Finite fault inversion

To constrain the rupture process of the mainshock, we selected 27 unclipped components of 10 regional broadband stations and 20 components of 10 local strong-motion stations based on the signal-to-noise ratio and azimuth coverage (Fig. S8). The epicentral distances of these stations ranged from 25 km to 241 km. The selected broadband regional seismic data were manually picked for the *P*-wave arrival time. After applying instrument response correction through deconvolution, the velocity records were integrated to derive displacement waveforms. The strong-motion seismic data were also manually picked for the *P*-wave arrival time but were integrated twice to displacement waveforms. Subsequently, we applied a Butterworth band-pass filter with a frequency range of 0.02 Hz–0.5 Hz to filter the displacement waveforms. We resampled all observed records to 0.1 s to match the interval of the synthetic data. The Green's function synthesis algorithm and velocity model maintain consistency with the computational framework employed for focal mechanism inversion. The observed and synthetic data were both cut using a time window of 10 s before and 51.2 s after the *P*-wave arrival.

The simulated annealing finite fault inversion method based on wavelet transform (Ji et al., 2002a,b) was employed to invert the rupture process of the mainshock of the Jinggu earthquake. According to the relocation of the Jinggu earthquake sequence (Wang et al., 2018) and our mainshock mechanism, we defined the strike angle of the fault plane as 150° and the dip angle as 76°. The dimension of the fault plane was 28 km along the strike direction and 16 km along the dip direction. The subfault size was 2 km × 2 km. The epicenter of the mainshock was a double-difference relocation result of 23.378°N and 100.475°E (Wang et al., 2018). The source depth was determined based on the best-fit depth of the focal mechanism, which is 5.2 km. The hypocenter was located on the 6th subfault in the strike direction and the 3rd subfault in the dip direction. The parameter space for the search (Hao et al., 2013, 2017; Chen et al., 2022, 2024) includes the slip ranging from 0 to 1.2 m, the rake angle between 149° and 209°, the rupture velocity ranging from 1.25 km/s to 3.75 km/s, and the rise time between 0.2 s and 1.2 s.

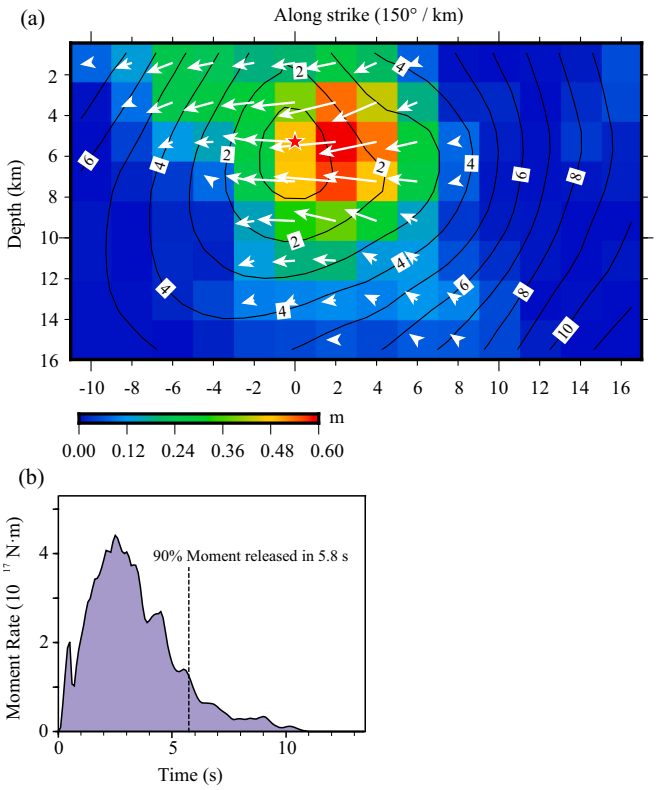

Fig. 4. The finite-fault inversion results of the mainshock. (a) The rupture process of the mainshock. The black contour and number denote the rupture front and the initial rupture time, respectively. The white arrows are the slip direction, and the color shows the slip value. (b) The moment rate of the mainshock.

Through the finite fault inversion, we obtained the rupture process of the Jinggu earthquake (Fig. 4). The inversion reveals that the moment magnitude is M_w 6.08, with a rupture scale of approximately 14 km along the strike direction and 16 km along the dip direction. The main rupture zone (with a slip amount greater than 0.48 m, MRZ) is located within a 4 km range in the 150° direction from the epicenter, at depths ranging from 6 km to 10 km, with a peak slip amount of 0.60 m. The fault motion direction is right-lateral strike-slip with bilateral rupture, with a weighted average rake angle of 182°, a weighted average rupture velocity of 1.89 km/s, and a weighted average rise time of 0.78 s. The waveform fitting of finite fault inversion is shown in Fig. 5.

5. Discussion and conclusions

The mainshock originated in a deep-seated ductile-brittle transition zone and propagated upward into a shallow brittle zone. According to our grid search and depth search results, the relocation of the mainshock's hypocenter was determined to be at 100.47°E, 23.40°N, and 9.3 km. The source location we obtained aligns well with the location determined by the relative positioning of Pn/Pg, which is 100.475°E, 23.384°N, at a depth of 9.5 km (Wang et al., 2019). The best-fit depth of 5.2 km reported in this study is in good agreement with the best-fit depth of 5.0 km obtained by using the CAP method (Wang et al., 2019). The source depth derived from the depth phases is regarded as the initial rupture depth of the earthquake. The best-fit depth serves as the geometric center of the MRZ. The rupture of the Jinggu earthquake was initiated from a deeper zone and propagated upward. The initial rupture occurred at the brittle-ductile transition zone (Scholz, 1998) with a depth of approximately 9.3 km. The depth of the brittle-ductile transition zone is consistent with the depth of the MRZ of the slip model (Fig. 4a). The deep-to-shallow rupture directivity and the rupture depth

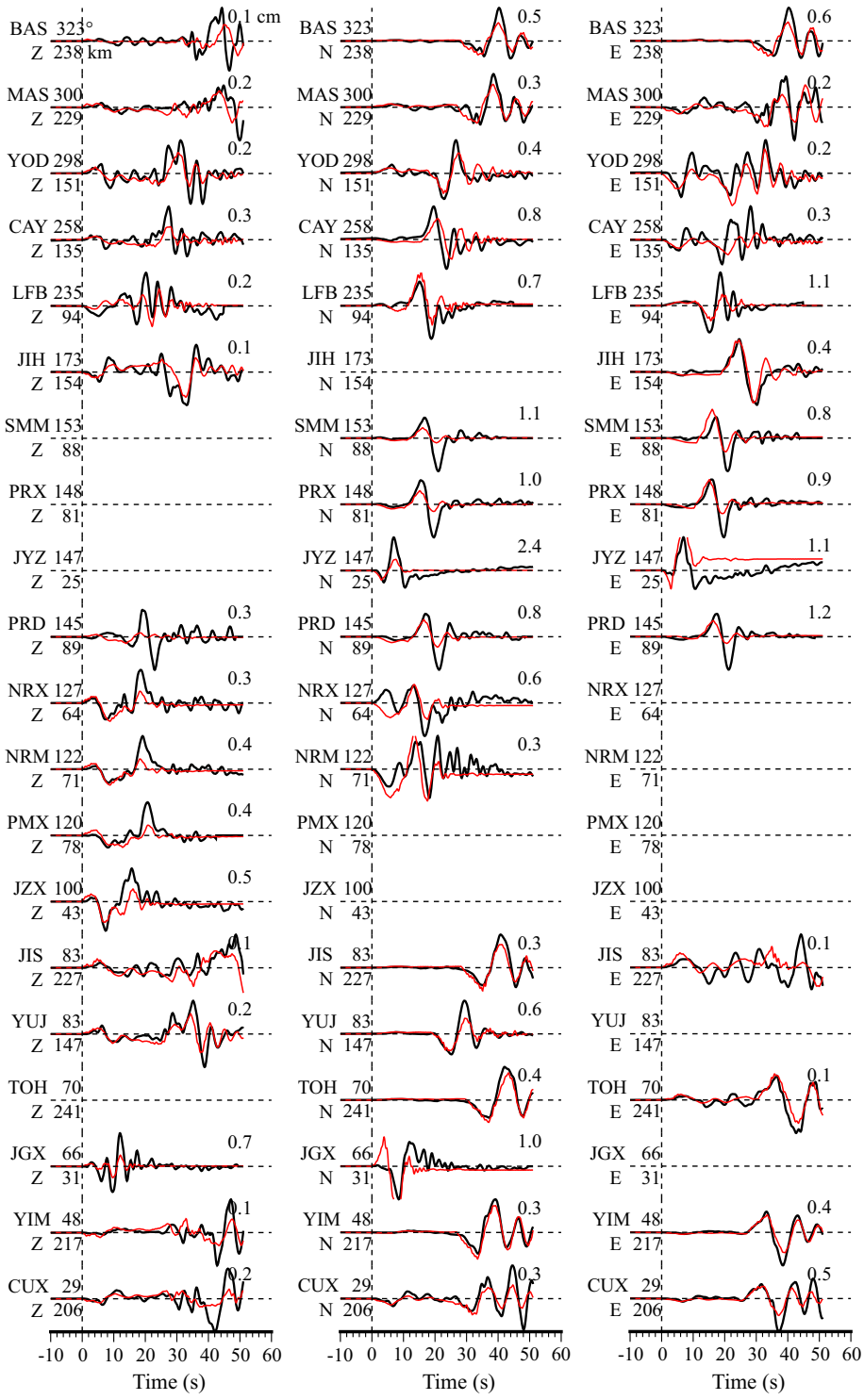

Fig. 5. The waveform fitting of the finite-fault inversion. The station name and azimuth (°) are marked on the top left of observed records (black) and synthetic waveforms (red). The component and epicentral distance (km) are denoted at the left bottom of waveforms. The numbers on the top right of waveforms are the peak amplitude values of waveforms with the unit in centimeters. (For interpretation of the references to color in this figure legend, the reader is referred to the web version of this article.)

extending into the brittle-ductile transition zone align with the conclusions of Wang et al. (2019).

The Jinggu earthquake sequence was a high-angle right-lateral strike-slip earthquake sequence. We statistically analyzed the dip angles of strike-slip earthquakes above M_w 4.0 in the Jinggu earthquake sequence. The statistical results reveal that the dip angles of eight strike-slip earthquakes above M_w 4.0 ranged from 63° to 84°, with an average dip angle of 78.75°. By analyzing the average dip angle of the seismic source mechanism in the Jinggu earthquake sequence, the results show that the seismogenic structure of this earthquake is a high-angle fault (Xie and Han, 2019). According to the analysis of the focal mechanism of the Ludian earthquake, it is suggested that the Ludian earthquake was also a high-angle earthquake, with the seismic source showing rapid energy release features (Chen et al., 2020). The rupture process of the

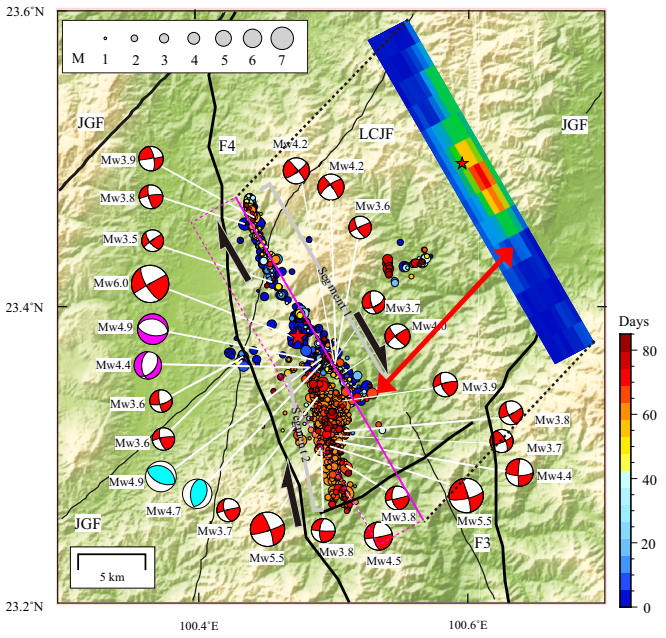

Fig. 6. The projection of the rupture process, the earthquake sequence, the focal mechanisms, and the moment rate of mainshock. The Jinggu earthquake sequence distribution (Wang et al., 2018) and focal mechanisms of $M > 3.5$ earthquakes are displayed. The magenta rectangular box denotes the fault plane of the mainshock. The color bar shows the days after the mainshock. The back lines are the same as the faults shown in Fig. 1. The red, purple, and cyan mechanisms are strike-slip earthquakes, formal earthquakes, and thrust earthquakes, respectively. (For interpretation of the references to color in this figure legend, the reader is referred to the web version of this article.)

Jinggu earthquake shows that 90 % of the energy is released within 0–5.8 s (Fig. 4b). The rapid energy release observed in the Jinggu earthquake was close to the energy release process of the Ludian earthquake, wherein 90 % of the energy of the Ludian earthquake is released within 2–13 s after the mainshock (Luo et al., 2018).

The Jinggu earthquake is an event of a single fault with bilateral rupture with approximately 4–9 km depth of MRZ (Fig. 4). The Jinggu earthquake sequence occurred on two fault segments. The mainshock sequence took place along a fault segment with a strike of 150° (Segment 1 in Fig. 6). The seismic sequence driven by two major M_W 5.5 earthquakes occurred along a fault segment (Segment 2 in Fig. 6) with a strike of 345°, 59 days after the mainshock. There is a strong correlation between the rupture scale of the mainshock and the distribution of the subsequent earthquake sequence on the fault Segment 1 (Fig. 6). Both the rupture process and the aftershock propagation stopped at the same location to the southeast point of Segment 1 (Fig. 6). The rupture propagation on Segment 2 (Fig. 6) may result from the mainshock's triggering of a sustained rupture along another fault plane within the conjugate fault system. The relationship between earthquake triggers is consistent with the conclusions drawn from the combination of paleoseismological trenching and numerical simulation methods (Sun et al., 2016). Statistical analysis of strike angles reveals distinct average values of 150° (Segment 1 in Fig. 6) and 343° (Segment 2 in Fig. 6), respectively. Based on the average strike angles of the two fault segments, we determined the rupture angle (φ in Fig. S7), which is the angle between the rupture surface and the maximum principal stress axis (Anderson, 1951). The rupture angle, when multiplied by two, is referred to as the fault conjugate angle; here, we obtained an approximate value of 13°. The fault conjugate angle of the Jinggu earthquake is smaller than the statistical range of 65° to 75° reported in other studies (e.g. Li et al., 2019; Wang and Chen, 2021). Therefore, we speculate that the fault segment 2 (Fig. 6) is an already existing buried fault, in which the mainshock rupture halted after triggering the rupture of segment 2 (Fig. 6), resulting in a single fault rupture. The single fault rupture and deep rupture zone of the Jinggu earthquake may be the main seismic factors contributing to its lesser impact in terms of disaster.

CRediT authorship contribution statement

Junlei Chen: Writing – review & editing, Writing – original draft, Visualization, Methodology, Formal analysis, Data curation, Conceptualization. **Yan Li:** Writing – review & editing, Writing – original draft. **Jinlai Hao:** Writing – review & editing, Supervision, Methodology, Funding acquisition. **Tao Xu:** Writing – review & editing, Supervision, Project administration, Funding acquisition.

Declaration of competing interest

The authors declare that they have no conflict of interest.

Acknowledgments

This work is supported by the National Natural Science Foundation of China [grant numbers 42104102, 42130807, 42074066] and the Kunming University of Science and Technology Talent Introduction Research Startup Fund Project (Natural Science Category) [grant number 141120240012]. We thank the International Earthquake Science Data Center (Doi:10.11998/IESDC), Yunnan Short-Period Reservoir Seismic Network Center, and Yunnan Earthquake Agency for providing the seismic data. We also thank Qingdong Wang for providing the aftershocks relocation catalog. Finally, I would like to thank the two reviewers for their constructive comments.

Appendix A. Supplementary data

Supplementary data to this article can be found online at https://doi.org/10.1016/j.pepi.2025.107410.

Data availability

The authors do not have permission to share data.

References

Anderson, E.M., 1951. The Dynamics of Faulting, Second ed. Oliver and Boyd, Edinburgh, Scotland. 206 pp.

Chang, Z., Chen, X., Chen, Y., Li, J., Lin, H., Hong, M., 2016. The co-seismic ground failure features and seismogenic structure of the Jinggu M_S 6.6 earthquake. Chin. J. Geophys. 59 (7), 2539–2552. https://doi.org/10.6038/cjg20160719 (in Chinese with English Abstract).

Chen, J., Zheng, Y., Zhang, L., Wu, Z., Hou, J., Guo, G., Liu, Y., Xu, T., Bai, Z., 2020. Focal mechanism solutions of the 2014 Ludian M_S 6.5 earthquake sequence derived from multiple-bandwidth waveform fitting. Chin. J. Geophys. 63 (4), 1472–1483. https://doi.org/10.6038/cjg2020N0386 (in Chinese with English Abstract).

Chen, J., Hao, J., Wang, Z., Xu, T., 2022. The 21 May 2021 M_W 6.1 Yangbi earthquake—a unilateral rupture event with conjugately distributed aftershocks. Seismol. Res. Lett. 93, 1382–1399. https://doi.org/10.1785/0220210241.

Chen, J., Hao, J., Xu, T., 2024. Complex conjugate rupture of the 2014 M_W 6.2 Ludian (Yunnan, China) earthquake. J. Asian Earth Sci. 260, 105972. https://doi.org/10.1016/j.jseaes.2023.105972.

Cheng, C., Wang, D., Yao, Q., Fang, L., Xu, S., Huang, Z., Liu, T., Wang, Z., Huang, X., 2023. The 2021 M_W 7.3 Madoi, China earthquake: transient supershear ruptures on a presumed immature strike-slip fault. J. Geophys. Res. Solid Earth 128 (2), e2022JB024641. https://doi.org/10.1029/2022JB024641.

Crotwell, H.P., Owens, T.J., Ritsema, J., 1999. The TauP Toolkit: flexible seismic travel-time and ray-path utilities. Seismol. Res. Lett. 70 (2), 154–160. https://doi.org/10.1785/gssrl.70.2.154.

Gong, W., Ye, L., Qiu, Y., Lay, T., Kanamori, H., 2022. Rupture directivity of the 2021 M_W 6.0 Yangbi, Yunnan earthquake. J. Geophys. Res. Solid Earth 127 (9), e2022JB024321. https://doi.org/10.1029/2022JB024321.

Guo, R., Li, L., Zhang, W., Zhang, Y., Tang, X., Dai, K., Li, Y., Zhang, L., Wang, J., 2023. Kinematic slip evolution during the 2022 M_S 6.8 Luding, China, earthquake: compatible with the preseismic locked patch. Geophys. Res. Lett. 50 (5), e2023GL103164. https://doi.org/10.1029/2023GL103164.

Hao, J., Ji, C., Wang, W., Yao, Z., 2013. Rupture history of the 2013 M_W 6.6 Lushan earthquake constrained with local strong motion and teleseismic body and surface

waves. Geophys. Res. Lett. 40, 5371–5376. https://doi.org/10.1002/2013GL056876.
Hao, J., Ji, C., Yao, Z., 2017. Slip history of the 2016 M_w 7.0 Kumamoto earthquake: intraplate rupture in complex tectonic environment. Geophys. Res. Lett. 44, 743–750. https://doi.org/10.1002/2016GL071543.
Ji, C., Wald, D.J., Helmberger, D.V., 2002a. Source description of the 1999 Hector Mine, California, earthquake, part I: wavelet domain inversion theory and resolution analysis. Bull. Seismol. Soc. Am. 92 (4), 1192–1207. https://doi.org/10.1785/0120000916.
Ji, C., Wald, D.J., Helmberger, D.V., 2002b. Source description of the 1999 Hector Mine, California, earthquake, part II: complexity of slip history. Bull. Seismol. Soc. Am. 92 (4), 1208–1226. https://doi.org/10.1785/0120000917.
Jia, H.C., Chen, F., Fan, Y.D., Pan, D.H., 2016. Comparison of two large earthquakes in China: the M_S 6.6 Yunnan Jinggu earthquake and the M_S 6.5 Yunnan Ludian earthquake in 2014. Int. J. Disaster Risk Reduct. 16, 99–107. https://doi.org/10.1016/j.ijdrr.2016.01.006.
Kanamori, H., 1977. The energy release in great earthquakes. J. Geophys. Res. 82 (20), 2981–2987. https://doi.org/10.1029/JB082i020p02981.
Kanamori, H., Anderson, D., 1975. Theoretical basis of some empirical relations in seismology. Bull. Seismol. Soc. Am. 65 (5), 1073–1095. https://doi.org/10.1785/BSSA0650051073.
Laske, G., Masters, G., Ma, Z., Pasyanos, M., 2013. Update on CRUST1. 0—A 1-degree global model of Earth's crust. Geophys. Res. Abstr. 15, EGU2013, 2658.
Li, Y., Wang, D., Xu, S., Fang, L., Cheng, Y., Luo, G., Yan, B., Enescu, B., Mori, J., 2019. Thrust and conjugate strike-slip faults in the 17 June 2018 MJMA 6.1 (M_w 5.5) Osaka, Japan, earthquake sequence. Seismol. Res. Lett. 90 (6), 2132–2141. https://doi.org/10.1785/0220190122.
Li, Y., Zhao, D., Shan, X., Gao, Z., Huang, X., Gong, W., 2022. Coseismic slip model of the 2022 M_w 6.7 Luding (Tibet) earthquake: pre- and post-earthquake interactions with surrounding major faults. Geophys. Res. Lett. 49 (24), e2022GL102043. https://doi.org/10.1029/2022GL102043.
Liang, H., Wu, Y., Shao, Z., Li, J., Li, Y., Yi, S., Yang, F., Zhuang, W., Wang, H., Zhan, W., Chen, C., 2023. Coseismic slip and deformation mode of the 2022 M_w 6.5 Luding earthquake determined by GPS observation. Tectonophysics 865, 230042. https://doi.org/10.1016/j.tecto.2023.230042.
Liu, C., Lay, T., Wang, R., Taymaz, T., Xie, Z., Xiong, X., Irmak, T.S., Kahraman, M., Erman, C., 2023a. Complex multi-fault rupture and triggering during the 2023 earthquake doublet in southeastern Türkiye. Nat. Commun. 14 (1), 5564. https://doi.org/10.1038/s41467-023-41404-5.
Liu, X., Xu, W., He, Z., Fang, L., Chen, Z., 2022. Aseismic slip and cascade triggering process of foreshocks leading to the 2021 M_w 6.1Yangbi earthquake. Seismol. Res. Lett. 93, 1413–1428. https://doi.org/10.1785/0220210263.
Liu, Y., Yu, Z., Zhang, Z., Yao, H., Wang, W., Zhang, H., Fang, H., Fang, L., 2023b. The high-resolution community velocity model V2.0 of southwest China, constructed by joint body and surface wave tomography of data recorded at temporary dense arrays. Sci. China Earth Sci. 66, 2368–2385. https://doi.org/10.1007/s11430-022-1161-7.
Luo, Y., Hsieh, M.C., Zhao, L., 2018. Source rupture process of the 2014 M_S 6.5 Ludian, Yunnan, China, earthquake in 3D structure: the strain green's tensor database approach. Bull. Seismol. Soc. Am. 108 (6), 3270–3277. https://doi.org/10.1785/0120180090.
Scholz, P.H., 1998. Earthquakes and friction laws. Nature 391, 37–42. https://doi.org/10.1038/34097.
Shi, F., He, H., Densmore, A.L., Bi, L., Wei, Z., 2016. Research on the relationship between fractal factors and tectonic activity-a case study of southwestern Yunnan block. Seismol. Geol. 38 (4), 862–873. https://doi.org/10.3969/j.issn.0253-4967.2016.04.005 (in Chinese with English Abstract).
Song, J., Chen, Y., Zhang, Y., 2020. Comparative study on the energy-moment ratio between the 2013 Minzhang earthquake and the 2014 Jinggu earthquake. Chin. J. Geophys. 63 (9), 3324–3337. https://doi.org/10.6038/cjg2020O0051 (in Chinese with English Abstract).
Sun, H., Jiang, G., He, H., Xu, X., Wei, Z., Gao, W., 2016. The influence of the 2014 Jinggu M_S 6.6 earthquake on the seismic risk of the Nantinghe fault zone in Yunnan province, China. Chin. J. Geophys. 59 (2), 180–189. https://doi.org/10.1002/cjg2.20224.
Wang, A., Chen, Y., 2021. A method of determination of the internal friction characteristics within the Earth's crust through conjugate earthquakes. Chin. J. Geophys. 64 (10), 3442–3451. https://doi.org/10.6038/cjg2021P0286 (in Chinese with English Abstract).
Wang, Q., Chu, R., Yang, H., Zhu, L., Su, Y., 2018. Complex rupture of the 2014 M_S 6.6 Jinggu earthquake sequence in Yunnan province inferred from double-difference relocation. Pure Appl. Geophys. 175, 4253–4274. https://doi.org/10.1007/s00024-018-1913-y.
Wang, S., Zeng, X., Wang, X., Wang, Q., 2019. Focal depth of the Yunnan Jinggu M_w 6.1 earthquake: discussion on depth of the brittle-ductile transition zone of a young fault. Chin. Sci. Bull. 64, 474–484. https://doi.org/10.1360/N972018-00678 (in Chinese with English Abstract).
Wen, X., Ma, S., Fang, L., Liang, M., Du, F., Long, F., Zhao, X., 2022. Complex structural fault system and distributed deformation across the Big Bend of the Red River fault, Yunnan, China. Phys. Earth Planet. Inter. 333, 106942. https://doi.org/10.1016/j.pepi.2022.106942.
Wu, J., Cai, Y., Wang, W., Wang, W., Wang, C., Fang, L., Liu, Y., Liu, J., 2024. Three dimensional velocity model and its tectonic implications at China Seismic Experimental Site, eastern margin of the Tibetan Plateau. Sci. China Earth Sci. 67 (7), 2268–2290. https://doi.org/10.1007/s11430-023-1293-4.
Xie, Z., Han, Z., 2019. Study on the seismogenic fault and dynamics parameters of the 2014 M_S 6.6 Jinggu earthquake in Yunnan. Seismol. Geol. 41 (4), 887–910. https://doi.org/10.3969/j.issn.0253-4967.2019.04.006 (in Chinese with English Abstract).
Xu, F., Liu, Z., Zhang, Z., Li, J., Liu, L., Su, Y., 2015. Double difference relocation and focal mechanisms of the Jinggu M_S 6.6 earthquake sequences in Yunnan province in 2014. Earth Sci. J. China Univ. Geosci. 40 (10), 1741–1754. https://doi.org/10.3799/dqkx.2015.156 (in Chinese with English Abstract).
Xu, P., Wen, R., Ren, Y., 2018. Comparison of strong-motion records and damage implications between the 2014 Yunnan M_S 6.5 Ludian earthquake and M_S 6.6 Jinggu earthquake. Earthq. Sci. 31 (1), 12–18. https://doi.org/10.29382/eqs-2018-0002-2.
Xu, X., Cheng, J., Xu, C., Li, X., Yu, G., Chen, G., Tan, X., Wu, X., 2014. Discussion on block kinematic model and future themed areas for earthquake occurrence in the Tibetan Plateau: inspiration from the Ludian and Jinggu earthquakes. Seismol. Geol. 36 (4), 1116–1134. https://doi.org/10.3969/j.issn.0253-4967.2014.04.015 (in Chinese with English Abstract).
Ye, L., Lay, T., Bai, Y., Cheung, K.F., Kanamori, H., 2017. The 2017 M_w 8.2 Chiapas, Mexico, earthquake: energetic slab detachment. Geophys. Res. Lett. 44 (23), 11,824–11,832. https://doi.org/10.1002/2017GL076085.
Yuan, J., Kao, H., Yu, J., 2020. Depth-scanning algorithm: accurate, automatic, and efficient determination of focal depths for local and regional earthquakes. J. Geophys. Res. Solid Earth 125 (7), e2020JB019430. https://doi.org/10.1029/2020JB019430.
Yue, H., Shen, Z., Zhao, Z., Wang, T., Cao, B., Li, Z., Bao, X., Zhao, L., Song, X., Ge, Z., Ren, C., Lu, W., Zhang, Y., Jing, L.Z., Wang, M., Huang, Q., Zhou, S., Xue, L., 2022. Rupture process of the 2021 M7.4 Maduo earthquake and implication for deformation mode of the Songpan-Ganzi terrane in Tibetan Plateau. Proc. Natl. Acad. Sci. 119 (23), e2116445119. https://doi.org/10.1073/pnas.2116445119.
Zhang, X., Feng, W., Du, H., Samsonov, S., Yi, L., 2022. Supershear rupture during the 2021 M_w 7.4 Maduo, China, earthquake. Geophys. Res. Lett. e2022GL097984. https://doi.org/10.1029/2022GL097984.
Zhang, Y., Chen, Y.T., Feng, W., 2019. Complex multiple-segment ruptures of the 28 September 2018, Sulawesi, Indonesia, earthquake. Sci. Bull. 64 (10), 650–652. https://doi.org/10.1016/j.scib.2019.04.018.
Zhu, L., Ben-Zion, Y., 2013. Parametrization of general seismic potency and moment tensors for source inversion of seismic waveform data. Geophys. J. Int. 194 (2), 839–843. https://doi.org/10.1093/gji/ggt137.
Zhu, L., Rivera, L.A., 2002. A note on the dynamic and static displacements from a point source in multilayered media. Geophys. J. Int. 148 (3), 619–627. https://doi.org/10.1046/j.1365-246X.2002.01610.x.